INDERSCIENCE PUBLISHERS
Linking academia, business and industry through research

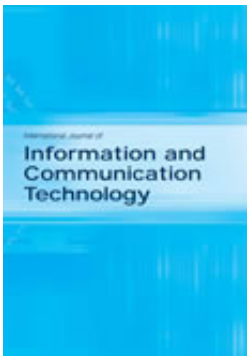

International Journal of Information and Communication Technology

ISSN online: 1741-8070 - ISSN print: 1466-6642
https://www.inderscience.com/ijict

Vulnerable sections identification of distribution networks based on hybrid graph neural networks

Junwei Zhu, Feng He, He Zhang, Jianbin Xu, Wei Lu, Ning Chen

DOI: 10.1504/IJICT.2026.10077274

Article History:

Received:	12 November 2025
Last revised:	16 December 2025
Accepted:	22 December 2025
Published online:	13 April 2026

Vulnerable sections identification of distribution networks based on hybrid graph neural networks

Junwei Zhu*, Feng He, He Zhang, Jianbin Xu, Wei Lu and Ning Chen

Putian Power Supply Company,
State Grid Fujian Electric Power Co., Ltd.,
Putian 351100, China
Email: zhujw@rsm.ac.cn
Email: 79063349@qq.com
Email: 1275339382@qq.com
Email: 979817964@qq.com
Email: luwei_2012@qq.com
Email: 848782127@qq.com
*Corresponding author

Abstract: Aiming at the voltage limit violations and line overloads caused by high-penetration renewable energy integration, this paper proposes a comprehensive identification method for weak links in distribution networks that integrates dual features of operational status and topological structure. A hybrid Copula function characterises the spatiotemporal correlation of photovoltaic output, and adaptive importance sampling generates typical scenarios. Probabilistic power flow calculates the violation probabilities of node voltage and line current. State and supply vulnerability indices based on utility functions are constructed to quantify voltage instability risk and nodal topological criticality, respectively. A graph neural network is then employed to integrate topological information for comprehensive weak-link identification. Simulation results based on the IEEE 33-node system demonstrate that the proposed method effectively combines operational and topological information, providing a reference for identifying weak links and optimising energy storage configuration in new-type distribution networks.

Keywords: hybrid Copula; probabilistic power flow; graph neural network; GNN; vulnerability identification; state vulnerability; structural vulnerability.

Reference to this paper should be made as follows: Zhu, J., He, F., Zhang, H., Xu, J., Lu, W. and Chen, N. (2026) 'Vulnerable sections identification of distribution networks based on hybrid graph neural networks', *Int. J. Information and Communication Technology*, Vol. 27, No. 32, pp.55–81.

Biographical notes: Junwei Zhu is a Senior Engineer with State Grid Putian Electric Power Supply Company. His research interests include distribution network operation and control, renewable energy generation power forecasting.

Feng He is a Senior Engineer with State Grid Putian Electric Power Supply Company. His research interests include distribution network operation and control.

He Zhang is an Engineer with State Grid Putian Electric Power Supply Company. His research interests include distribution network operation and control.

Jianbin Xu is an Engineer with State Grid Putian Electric Power Supply Company. His research interests include distribution network operation and control.

Wei Lu is an Engineer with State Grid Putian Electric Power Supply Company. His research interests include distribution network operation and control.

Ning Chen is an Engineer with State Grid Putian Electric Power Supply Company. His research interests include distribution network operation and control.

1 Introduction

With the deepening advancement of the 'dual-carbon' goals, the widespread integration of high-penetration distributed photovoltaic (DPV) systems into distribution networks, while enhancing renewable energy accommodation capacity, has also introduced new operational challenges such as voltage limit violations, reverse power flow, and reduced system inertia (Yang et al., 2024; Dong et al. 2021). The randomness, intermittency, and spatial correlation of photovoltaic (PV) output have profoundly altered the traditional fault characteristics and operational mechanisms of distribution networks, leading to a stronger spatiotemporal coupling and uncertainty in the distribution of system vulnerable sections (Yan et al., 2024). Against this backdrop, traditional deterministic power flow-based 'N-1' security verification methods struggle to effectively assess the operational risks arising from such stochasticity. Therefore, there is an urgent need to develop new methods capable of accurately identifying multi-dimensional vulnerable sections in distribution networks, providing a decision-making basis for the planning, operation, and active defence of active distribution networks (Yang et al., 2025a).

Current research on PV output correlation and vulnerable section identification in distribution networks with high-penetration DPV has achieved a series of advancements. Chen et al. (2022b) proposed an innovative risk-resilience dual-dimensional assessment framework for identifying vulnerable sections in integrated energy systems, employing the cumulant method to achieve efficient probabilistic multi-energy flow calculation, significantly improving assessment speed and practicality. However, the study did not consider the spatiotemporal correlation between wind and PV power outputs, which can affect the accuracy of the risk probability distribution in scenarios with high renewable energy penetration. Bao et al. (2023) effectively characterised the correlation between wind speed and blade load using a Copula function and constructed a prediction model. Tao (2024) proposed a method combining a hybrid Copula function with multivariate normal distribution to generate wind-PV output scenarios considering dynamic correlation, thereby more accurately characterising the uncertainty and coupling effects of wind and PV power. Duan et al. (2019) introduced dynamic Copula theory into joint wind-PV output modelling, using a dynamic Copula model to more precisely capture the

time-varying patterns and asymmetric tail dependence characteristics of wind and PV output.

Existing research primarily unfolds along three directions: Methods based on network topology (e.g., complex network theory) focus on static structural characteristics and propose indicators such as node degree and betweenness centrality, but fail to effectively integrate dynamic operational state changes. Chen et al. (2022a) systematically reviewed the application of complex network theory in bulk power grid vulnerability assessment, proposing topological indicators like node degree and betweenness centrality. Zhang et al. (2021) integrated complex network theory with operational risk theory, proposing a dynamic identification method based on node criticality; Wang et al. (2021) further considered the stochastic characteristics of distributed generation output, refining node degree and betweenness indicators to enhance the adaptability of topological vulnerability assessment. Methods based on operational characteristics (e.g., voltage stability analysis) rely on deterministic or simple probabilistic power flow. While they can reflect the risk of electrical quantity violations, they insufficiently account for the complex dependencies of PV output. Xu et al. (2020) employed the unscented transformation method for probabilistic analysis of distribution network voltage stability indicators, quantifying violation risk; Yang et al. (2025b) conducted static voltage stability analysis in renewable-integrated grids considering distributed static series compensator (DSSC). Yu et al. (2024) proposed a multi-level reverse overloading risk assessment framework for high-penetration PV integration scenarios. Zhang et al. (2023) focused on DC zonal distribution networks, analysing their voltage stability mechanisms.

Data-driven methods (e.g., random matrix theory, machine learning) avoid the complexity of physical modelling, but their black-box nature leads to poor interpretability of results and dependence on high-quality measurement data. Wang et al. (2022) achieved the identification of weak points in integrated energy systems based on unified power flow big data. Zeng et al. (2020) utilised a double Q-learning algorithm, considering transient stability constraints, to achieve intelligent identification of weak lines in the power grid. Yan and Li (2024) constructed an outlier-immune data-driven linear power flow model, automatically excluding bad data through mixed-integer programming, improving the power flow calculation accuracy for distribution networks with missing models. Yan and Xu (202) combined Gaussian mixture model (GMM) with Copula function to model the dependency structure between PV plant outputs, effectively characterising the joint distribution characteristics of stochasticity.

In summary, existing methods still exhibit significant limitations regarding the integration of dynamic operational and static structural features, the fine-grained modelling of PV output correlation, and the interpretability of the assessment process. To address the aforementioned issues, this study proposes an intelligent identification framework based on graph neural networks (GNNs) that integrate dual state and structural features, focusing on overcoming two key challenges: PV output modelling and multi-dimensional feature fusion. First, hybrid Copula theory is adopted to accurately characterise the nonlinear and tail dependence characteristics of PV output, and adaptive importance sampling is used to generate typical scenarios. Subsequently, a comprehensive evaluation indicator system is constructed from both state and structural dimensions to quantify operational risk and topological criticality. Finally, the distribution network is abstracted as a graph structure, the dual vulnerability indicators are used as node and edge features, and a GNN model is constructed to achieve end-to-end accurate identification of vulnerable sections.

2 Typical scenario generation for PV output based on hybrid Copula

2.1 Correlation analysis of PV output based on hybrid Copula function

PV output is affected by multiple factors, including solar irradiance, cloud cover variations, temperature, and equipment performance. Its probability distribution often deviates from the classical normal distribution, exhibiting complex characteristics such as multimodality and skewness. To accurately describe its statistical properties, this paper employs the empirical distribution function (EDF) method to model the marginal distribution of PV output. For a PV output sequence containing independent and identically distributed samples, the EDF is defined as:

$$F_n(x) = \frac{\text{Number of samples less than or equal to } x}{n} \tag{1}$$

A multivariate joint distribution can be determined by its marginal distributions and a Copula function that captures the dependency structure among the variables (Zhu et al., 2019):

$$H(x, y) = C\big(F(x), G(y)\big) \tag{2}$$

where $F(x)$ and $G(y)$ are the marginal distributions of variables x and y, and $C(u, v)$ is a Copula function that characterises the dependency structure between x and y.

A hybrid Copula function is constructed as a linear combination of four Copula types. Their corresponding probability density functions can be expressed as:

$$\begin{aligned} C_{mix}(u, v; \theta) = {} & \omega_{clayton} C_{clayton} + \omega_{gumbel} C_{gumbel} \\ & + \omega_{frank} C_{frank} + \omega_{gaussian} C_{gaussian} \end{aligned} \tag{3}$$

where $C_{clayton}$ denotes the Clayton Copula function, which is adept at capturing lower tail dependence and precisely characterises the risk of simultaneous low-output events across PV power plants during adverse weather conditions; C_{gumbel} represents the Gumbel Copula function, which excels in modelling upper tail dependence and is suitable for describing the synergy in high-output generation between two plants under clear weather; C_{frank} is the Frank Copula function, proficient in capturing symmetric dependence and applicable to the correlation patterns observed during moderate output conditions; and $C_{gaussian}$ signifies the Gaussian Copula function, which effectively captures overall linear and nonlinear correlation structures but lacks tail dependence. The coefficients are the weights assigned to each component, satisfying $\sum \omega_i = 1$, and θ denotes the set of all parameters to be estimated.

We employ the EM algorithm to estimate the weighting coefficients of the mixture Copula function. To ensure the convergence of the EM algorithm:

- Initialisation: The initial weights for the four Copula components are set equally to 0.25. Their initial parameters are derived from method-of-moments estimates based on the transformed uniform data, providing a stable starting point.

- Convergence criterion: The iteration stops when the relative improvement in the log-likelihood $\mathcal{L}$ between consecutive iterations falls below a tolerance of 10^{-6}, i.e., $\left|\mathcal{L}^{(t)} - \mathcal{L}^{(t-1)}\right| / \left|\mathcal{L}^{(t-1)}\right| < 10^{-6}$.
- Stopping rule: A maximum of 500 iterations is set as a safeguard. In practice, convergence is typically achieved within 100–150 iterations.

2.2 Correlation-based scenario generation for PV output using adaptive importance sampling

The core concept of importance sampling is to draw samples indirectly from a target $p(u_i)$ distribution by using a known and easily sampled proposal distribution $q(u_i)$. Each sample u_i drawn from $q(u_i)$ is assigned an importance weight ω_i to correct for the bias between the two distributions. A larger weight indicates a higher relative probability of the sample occurring under the target distribution, signifying its greater importance. The importance weight is defined as:

$$\omega_i = \frac{p(u_i)}{q(u_i)} \tag{4}$$

The performance of the importance sampling method is highly dependent on the choice of the proposal distribution. A fixed proposal distribution $q(u_i)$ often fails to accurately match the joint probability distribution of PV output. This mismatch leads to a large number of samples falling into low-probability regions, resulting in low sampling efficiency and consequently a conservative bias in system risk assessment. An adaptive importance sampling approach is developed to dynamically adjust and optimise the proposal distribution. Resampling techniques are then employed to extract N independent, equally weighted samples from the set of weighted samples, which best represent the target distribution, thereby forming an initial scenario set.

2.3 PV scenario reduction based on GMM

The GMM is a probabilistic soft clustering method whose Gaussian component parameters are estimated via the expectation-maximisation (EM) algorithm. The mean vector $\boldsymbol{\mu}_k$ of each Gaussian component obtained through clustering is regarded as a typical scenario, with its coordinates representing the PV output values of all plants under that scenario. Assuming all data points are generated from a mixture of multiple Gaussian distributions, the probability density function can be expressed as:

$$p(x) = \sum_{k=1}^{K} \phi_k \cdot \mathcal{N}\left(\mathbf{x} \mid \boldsymbol{\mu}_k, \boldsymbol{\Sigma}_k\right) \tag{5}$$

where K is the number of Gaussian components (i.e., clusters), ϕ_k is the mixing weight of the k^{th} Gaussian component, satisfying $\sum_{k=1}^{K} \phi_k = 1$, and $\boldsymbol{\mu}_k$ and $\boldsymbol{\Sigma}_k$ are the mean vector and covariance matrix of the k^{th} component, respectively. $\mathcal{N}(\mathbf{x} \mid \boldsymbol{\mu}_k, \boldsymbol{\Sigma}_k)$ denotes the probability density of observing data point x given the mean $\boldsymbol{\mu}_k$ and covariance matrix $\boldsymbol{\Sigma}_k$.

By integrating adaptive importance sampling with GMM clustering, the complex continuous joint distribution is transformed into a discrete set Ω of typical scenarios, each with probabilistic significance:

$$\Omega = \left\{ (S_k, \pi_k) \mid k = 1, 2, ..., K \right\} \tag{6}$$

where K is the total number of typical scenarios, S_k is the k^{th} typical scenario (a vector representing the output values of all PV plants in this scenario), and π_k is the probability of occurrence of the k^{th} typical scenario, satisfying $\sum_{k=1}^{K} \pi_k = 1$.

3 Construction of a comprehensive assessment indicator system for distribution network vulnerability

The integration of high-penetration DPV systems results in complex vulnerability characteristics in distribution networks, where dynamic operational risks intertwine with inherent structural weaknesses. To address the limitations of single-dimensional assessments, a comprehensive indicator system is developed from two perspectives: state vulnerability and structural vulnerability. State vulnerability focuses on the real-time risk of component operational limit violations, while structural vulnerability reveals the inherent weaknesses of network topology and parameters. By establishing a comprehensive indicator system, the systemic vulnerability induced by large-scale PV integration is quantified, enabling the identification of weak components in distribution networks.

3.1 State vulnerability assessment indicators

State vulnerability assessment quantifies the risk of key parameters (e.g., voltage, current) exceeding safety limits under current or expected conditions. Following the definition of risk as 'likelihood multiplied by consequence severity,' the limit-violation risk indicator is defined as the product of violation probability and vulnerability severity. A method for quantifying vulnerability severity is developed based on improved repetitive power flow and utility theory. To quantify a component's ability to maintain voltage and current within safe limits under load growth or distributed generation power fluctuations, this paper employs an improved repetitive power flow method to determine the maximum power supply capacity at each node. This involves iteratively calculating the maximum multiplier $k_{\max}$ by which the system nodal load can be increased while satisfying all security constraints.

An 'increasing marginal risk' phenomenon exists in power systems. As available supply capacity decreases, its marginal value rises and the consequences of loss become more severe. Since the power supply capacity increment L_{out} is an absolute quantity, this paper introduces a risk-seeking utility function from utility theory to map the vulnerability severity indicator. This transforms L_{out} into a relative vulnerability severity indicator that reflects the 'increasing marginal risk' effect. The mapping function is expressed as follows:

$$Q = u(L_{out}) = \frac{1}{c}\left(\exp\left[a(L_{out} + b)\right] - 1\right) \tag{7}$$

where $a = 0.5$, $b = 0.2$ and $c = 1$ are shape parameters of the function.

A smaller b value ensures that the function $f(\Delta P)$ exhibits relatively gradual changes when the increment ΔP in supply capacity is small, thereby avoiding excessive sensitivity to minor variations. Meanwhile, setting a to 0.5 as a scaling factor adjusts the output to an appropriate magnitude. Setting c to 1 ensures that when ΔP is large (i.e., sufficient power supply capacity), the vulnerability severity does not drop to zero but converges to a low baseline value. This aligns with the engineering principle that fundamental risks persist even when ample margins exist. This set of parameters is designed to concisely reflect, in mathematical form, the physical intuition that 'the smaller the remaining power supply capacity, the higher its marginal value and the more severe its vulnerability.' Their specific values are determined through calibration against typical system data, enabling effective capture of the risk's nonlinear characteristics.

The state vulnerability risk index R for a component (node i, branch l) is determined by both its violation probability P and its vulnerability severity Q:

$$\begin{aligned} R_{V,i} &= P_{V,i} \cdot Q_{V,i} = P_{V,i}\left(\exp L_{out,i} - 1\right) \\ R_{I,l} &= P_{I,l} \cdot Q_{I,l} = P_{I,l}\left(\exp L_{out,l} - 1\right) \end{aligned} \tag{8}$$

In the equation, the violation probabilities $P_{V,i}$ and $P_{I,i}$ are obtained from the probabilistic power flow analysis using the aforementioned cumulant method. This risk index R yields a comprehensive measure that integrates both the likelihood and the severity of potential violations. A higher index indicates greater vulnerability, suggesting that the component should be prioritised for monitoring and reinforcement.

3.2 Structural vulnerability assessment indicators

Structural vulnerability assessment aims to identify components that, due to their own failure or disconnection, significantly impact system connectivity and power supply reliability from the perspectives of network topology and parameters. Indicators such as node degree, injection power, and betweenness centrality are employed for structural vulnerability assessment.

3.2.1 Node structural indicators

a Node degree indicator $D_{N,i}$

The node degree indicator represents the number of lines directly connected to a given node and is used to identify critical connection points within the network. It is expressed as:

$$D_{N,i} = \frac{D_i}{\overline{D}} \sum_{j \in \psi_i} D_j \tag{9}$$

where D_i is the degree of node i, $\overline{D}$ is the average degree of the network, and ψ_i dis the set of neighbours of node i.

b Node injection power indicator $N_{p,i}$

Node injection power represents the active power magnitude at a node, reflecting its average transmission level under various scenarios. A larger value implies higher structural importance in power transmission. It can be expressed as:

$$N_{P,i} = \frac{1}{S_b} \sum_{s=1}^{n} \lambda_s P_{i,s} \tag{10}$$

where S_b is the base power, and $p_{i,s}$ is the injected active power at node i under scenario S.

c Node betweenness indicator $B_{N,i}$

Node betweenness centrality measures how often a node acts as an intermediate bridge along the shortest paths between other nodes. It reflects node criticality within the network; failure of a high-betweenness node may cause fragmentation or large-scale outages. Node betweenness can be expressed by the following formula:

$$B_{N,i} = \sum_{j \neq k \neq i} \frac{\sigma_{jk}(i)}{\sigma_{jk}} \tag{11}$$

where σ_{jk} is the number of shortest paths between node j and node i, and $\sigma_{jk}(i)$ is the number of those paths that pass through node i.

3.2.2 Line structural indicators

a Line degree indicator $D_{L,n}$

The concept of node degree is extended to lines, where line degree reflects electrical distance and the structural importance of its terminal nodes. It can be expressed as:

$$D_{L,n} = \frac{Z_n}{\overline{D}} \sqrt{D_{N,i} \cdot D_{N,j}} \tag{12}$$

where Z_n is the magnitude of the impedance of line n, and $D_{N,i}$ and $D_{N,j}$ are the degree indicators of its two terminal nodes.

b Line supply vulnerability indicator $H_{L,n}$

Based on line impedance and network topology, the line supply vulnerability indicator quantifies a line's structural criticality within the distribution network. Lines with lower impedance and higher restorable load exhibit lower supply vulnerability and greater structural importance. By jointly considering electrical attributes and post-fault system performance, this indicator overcomes the limitations of traditional complex network theory in radial systems. It provides a new dimension with clear physical significance for assessing line vulnerability. It can be expressed as:

$$H_{L,n} = \frac{K \cdot n_R}{Z_n + \varepsilon} \tag{13}$$

where K is the load level coefficient that the system can maintain after a line break, n_R is the theoretical number of load points that can be restored after a line break (estimated based on network connectivity), Z_n is the magnitude of the line impedance, and ε is a minimal constant to avoid zero errors.

Z_n (line impedance): Reflects the line's inherent electrical strength. A higher Z_n typically indicates lower thermal capacity and higher electrical losses, signalling greater intrinsic vulnerability. n_R (restorable load points): Determined by network topology and load distribution. It quantifies the number of loads that can be restored via alternative paths (e.g., tie lines) after the line's outage, representing the grid's redundancy.

Significance: A low value of $H_{L,n}$ identifies a line that is both electrically weak (high Z_n) and critically located for supply (low n_R). These lines are structural bottlenecks whose failure would cause severe and prolonged outages, prioritising them for reinforcement.

c Line betweenness indicator $B_{L,n}$

Line betweenness measures the number of times a line appears in all electrical shortest paths, reflecting its importance in power transmission. It can be expressed as:

$$B_{L,n} = \sum_{s} \lambda_s \frac{P_{s,n}}{p_{n,\max}} I_{s,n} \tag{14}$$

where $P_{s,n}$ is the transmission power of line in scenario s, $P_{n,\max}$ is its maximum transmission capacity, and $I_{s,n}$ is the indicator function.

4 Comprehensive identification of vulnerable sections in distribution networks based on GNNs

State and structural vulnerability indicators characterise network vulnerabilities at different levels under various operating conditions; however, they differ greatly in dimension and meaning. Traditional methods struggle to effectively integrate such heterogeneous information and are even less capable of capturing the complex coupling relationships inherent in the network topology. GNNs are inherently capable of processing graph-structured data, and their message-passing mechanism can simulate the propagation and mutual influence of power flows within distribution networks. Accordingly, a comprehensive GNN-based method is developed for identifying vulnerable sections in distribution networks. Leveraging the representation-learning capability of GNNs, the proposed method integrates topological and operational features to achieve precise, synergistic identification of dual state-structure vulnerabilities.

The overall technical workflow of the method proposed in this chapter is illustrated in Figure 1. Its core involves abstracting the distribution network into a graph structure and utilising a GNN model for node-level classification, ultimately outputting the vulnerability type for each node.

Figure 1 Flowchart of vulnerability identification based on GNNs

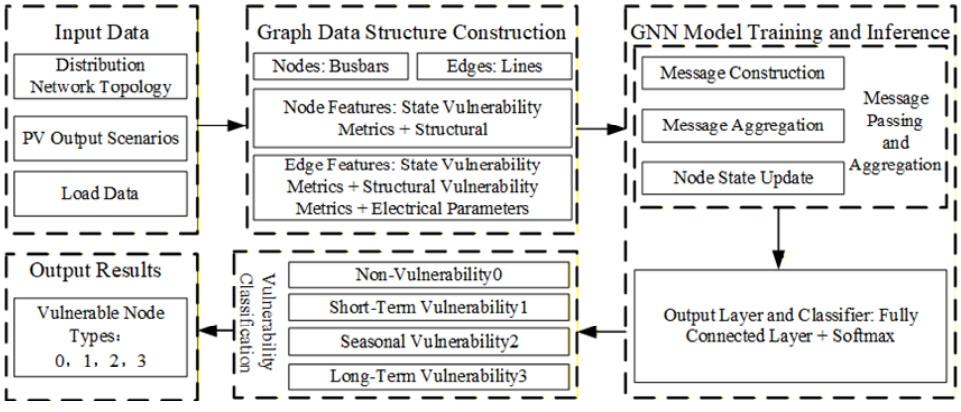

4.1 Construction of the distribution network graph data structure

The input to a GNN is inherently graph-structured, which naturally aligns with the topology of a distribution network. Therefore, utilising a GNN to map the distribution network into a graph structure naturally aligns with the physical connectivity properties of the power grid (Hu et al., 2023; Liu, 2012; Sun et al., 2022; Wang et al., 2024. In the GNN framework, the distribution network is fully represented as an attributed graph $G = (X, E, Y)$, which includes graph nodes, graph edges, and graph labels.

To ensure consistency and numerical stability of the model input, all node features x_i and edge features $e_{i,j}$ are normalised using Min-Max scaling before being fed into the GNN. For a feature x with N samples, its normalised value $\hat{x}$ is calculated as:

$$\hat{x} = \frac{x - x_{\min}}{x_{\max} - x_{\min}} \tag{15}$$

where $x_{\min}$ and $x_{\max}$ are the minimum and maximum values of that feature in the training set, respectively. This preprocessing step mitigates the influence of differing scales among features (e.g., voltage magnitudes vs. topological indices) and accelerates model convergence.

Each bus in the distribution network is defined as a graph node. The features of each node can be represented by a feature vector $x_i = [R_{V,i}, D_{N,i}, N_{P,i}, B_{N,i}]^T$, which integrates state and structural indicators of the distribution network. Where $R_{V,i}$ is the node voltage violation risk (a state indicator), $D_{N,i}$, $N_{P,i}$, $B_{N,i}$ are its degree, injection power, and betweenness indicators.

The lines in the distribution network are defined as edges connecting two nodes. Each edge is associated with a feature vector: $e_{i,j} = [R_{I,ij}, D_{L,ij}, H_{L,ij}, B_{L,ij}, r_{ij}, x_{ij}]^T$, which characterises electrical properties and structural indicators. $R_{I,ij}$ is the line current violation risk, $D_{L,ij}$, $H_{L,ij}$, $B_{L,ij}$ are the structural indicators, r_{ij}, x_{ij} are the line resistance and reactance. Each node is assigned a label $y_i = \{0, 1, 2, 3\}$, representing its vulnerability type (0: non-vulnerable, 1: short-term vulnerable, 2: seasonally vulnerable, 3: long-term vulnerable). These labels are derived from the statistical classification of historical node violation days in operational and maintenance data. Non-vulnerable (0): violation days ≤ 5%; short-term vulnerable (1): 5% < violation days ≤ 20%; seasonally vulnerable (2):

20% < violation days ≤ 50%; long-term vulnerable (3): violation days > 50%. This classification uses an annual time scale to capture patterns influenced by seasonal variations in PV output and load, providing a practical basis for maintenance planning.

4.2 GNN identification model design and message passing mechanism

The proposed model adopts the message-passing paradigm, enabling nodes to gather information from their topological neighbours through neighbourhood aggregation. This mechanism effectively captures the propagation and mutual influence of power flows within the grid, closely mirroring the physical reality where local disturbances propagate through lines in a distribution network.

The core of the GNN model consists of stacked graph convolution operations across L layers. Each layer performs one iteration of message passing, aggregation, and update, allowing the representation of each node to incorporate information from its neighbourhood.

First, during the message construction step at layer l for each edge connecting node u, v, a message is generated to be sent from the neighbouring node u to the target node v. The message function is defined as follows:

$$\mathbf{m}_{u\to v}^{(l)} = \mathrm{MLP}^{(l)}\left(\mathrm{CONCAT}\left(\mathbf{h}_u^{(l-1)}, \mathbf{e}_{uv}\right)\right) \tag{16}$$

where $\mathbf{h}_u^{(l-1)}$ is the feature vector of neighbouring node u at layer $l-1$, $\mathbf{e}_{uv}$ is the feature vector of edge (u, v), denotes vector concatenation, MLP(i) and is a trainable multilayer perceptron. This mechanism allows the model to simultaneously learn the complex relationships between node states, line attributes, and topological connections.

Next, the messages are aggregated. An average aggregation function is used to summarise all information received by the target node u from its neighbouring nodes into a combined neighbourhood message:

$$\tilde{m}_v^{(l)} = \frac{1}{|\mathcal{N}(v)|}\sum_{u\in\mathcal{N}(v)} \mathbf{m}_{u\to v}^{(l)} \tag{17}$$

This step simulates the comprehensive influence of neighbouring nodes on the target node and is key to capturing local network effects.

Finally, the node state is updated. The target node combines its own state from the previous layer with the aggregated neighbourhood message to update its state representation:

$$\mathbf{h}_v^{(l)} = \sigma\left(\mathbf{W}^{(l)}\cdot\mathrm{CONCAT}\left(\mathbf{h}_v^{(l-1)}, \tilde{m}_v^{(l)}\right) + \mathbf{b}^{(l)}\right) \tag{18}$$

where $W^{(l)}$ and $b^{(l)}$ are trainable weight matrices and bias vectors, respectively, and σ is a nonlinear activation function. After L such operations, the final representation $h_i^{(L)}$ of each node incorporates rich information from its L-hop neighbourhood, forming a deep feature representation that encompasses both its own 'state-structure' characteristics and the global topological context of the network. This explains why GNNs outperform traditional methods in accurately identifying vulnerable sections.

4.3 Output layer and vulnerability classification identification

After L layers of graph convolution, each node obtains a final representation $h_v^{(L)}$ containing rich local and global information. This representation is fed into a fully connected layer, and then the node's vulnerability type probability distribution is obtained through the Softmax function:

$$\hat{y}_v = \text{Softmax}\left(\mathbf{W}^{\text{out}}\mathbf{h}_v^{(L)} + \mathbf{b}^{\text{out}}\right) \tag{19}$$

where $\hat{y}_v$ is a four-dimensional vector, representing the probability that node belongs to the 'non-vulnerable', 'short-term vulnerable', 'seasonally vulnerable', and 'long-term vulnerable' categories, respectively. The model's identification result takes the category with the highest probability as the final vulnerability type for that node. Thus, an end-to-end process is established, mapping multi-dimensional heterogeneous input data to specific vulnerability classifications via the GNN model.

4.4 Model training and optimisation

1 Data splitting: A time-series splitting strategy is adopted for the training and testing data to validate the model's generalisation capability across the time dimension. Training set: Uses the full year 2020 distribution network operation data, containing node and line feature data under a total of 8,760 time snapshots. Test set: Uses the full year 2021 data as an independent test set to evaluate the model's performance on data from an unseen year.

2 Loss function: This paper employs a weighted cross-entropy loss function. By assigning higher weights to minority classes, the model is forced to focus on key categories with fewer samples. Based on the label distribution of the training set, the sample count for each category is counted, and the class weight $w_c = \frac{1}{N_c}$ is calculated and normalised:

$$w_c = \frac{1/N_c}{\sum_{c=1}^{C}(1/N_c)} \tag{20}$$

where C is the number of actual existing categories. The loss function is defined as:

$$\mathcal{L} = -\frac{1}{N}\sum_{v=1}^{N}\sum_{c=1}^{C} w_c \cdot y_{v,c}\log\left(\hat{y}_{v,c}\right) \tag{21}$$

where N is the total number of nodes, $y_{v,c}$ is the one-hot encoding of the true label, and $\hat{y}_{v,c}$ is the predicted probability.

3 Optimiser: The adaptive moment estimation (Adam) optimiser is used for parameter updates. Its automatic learning rate adjustment mechanism effectively accelerates convergence and improves training stability. Hyperparameter tuning: The key hyperparameters of the GNN model, including the initial learning rate, hidden layer

dimension, dropout rate, and weight decay coefficient, were determined through a structured tuning process. Based on common practices in training deep GNNs and preliminary experiments, we defined the following search space: learning rate $\eta \in \{0.001, 0.005, 0.01\}$, hidden dimension $d_{hidden} \in \{64, 128, 256\}$, dropout rate $p_{drop} \in \{0.1, 0.3, 0.5\}$, and weight decay $\lambda \in \{1 \times 10^{-5}, 1 \times 10^{-4}, 5 \times 10^{-4}\}$.We employed grid search coupled with five-fold cross-validation on the training dataset (year 2020 data) to evaluate each configuration. The performance was assessed using the macro-averaged F1-score on the validation folds to account for class imbalance.

The optimal configuration that emerged from this search was: initial learning rate $\eta = 0.005$, hidden dimension $d_{hidden} = 128$, dropout rate $p_{drop} = 0.3$, and weight decay $\lambda = 1 \times 10^{-4}$. This combination achieved the best trade-off between learning speed (convergence), generalisation performance (validation F1-score), and robustness against overfitting. The selected learning rate is slightly higher than a typical default, which we found beneficial for efficient convergence given our dataset size and model architecture, while the chosen weight decay effectively regularises the model parameters.

Final training setup: With the optimised hyperparameters, the model was trained using the Adam optimiser with momentum parameters $\beta_1 = 0.9$ and $\beta_2 = 0.999$. A fixed number of 200 training epochs was set, and training loss and accuracy were logged every 10 epochs to monitor performance.

4 Training procedure: The model is trained using full-batch training on the entire graph. The core process involves iterative forward propagation, loss computation, backward propagation, and parameter update. In each training epoch, the entire training set graph data, including node and edge features, is first input into the model for forward propagation to obtain predictions. Subsequently, the weighted cross-entropy loss between the predicted values and the true labels is calculated. Then, the gradients of the loss function with respect to all model parameters are computed via the backpropagation algorithm, and the Adam optimiser uses these gradients to update the parameters to minimise the loss. To evaluate the model's generalisation ability in real-time and achieve optimal model selection, performance is evaluated on the independent test set after each training epoch. The test accuracy is used as the core evaluation criterion, and the best-performing model parameters are continuously saved, thereby ensuring that the final obtained model possesses optimal identification accuracy and generalisation performance.

5 Case study

A simulation analysis was conducted based on the IEEE 33-node system, as shown in Figure 2. The distribution transformer had a rated capacity of 10 MVA, and the total load is 3.72 MW + 2.29 Mvar. PV systems were connected at nodes 16 and 26. The output range of PV1 was [0, 1.53] MW, and that of PV2 was [0, 2.38] MW.

Figure 2 Structure of the IEEE 33-bus distribution network system (see online version for colours)

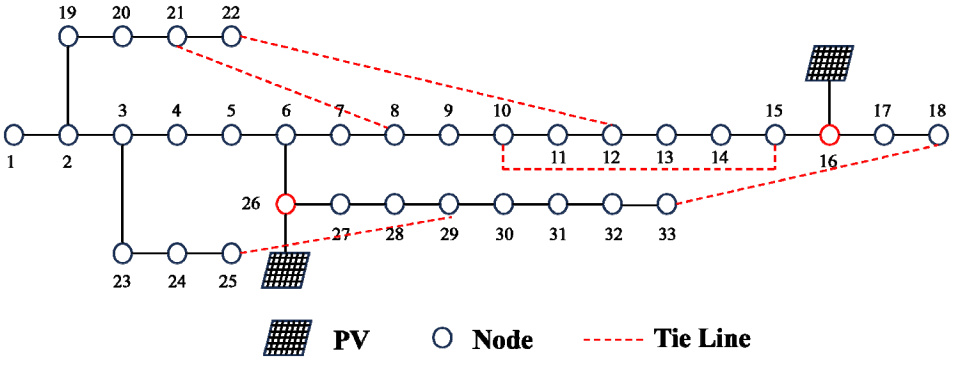

5.1 *Correlation analysis of PV output and scenario generation*

Based on annual operational data from real PV plants, a hybrid Copula model was employed to analyse their spatiotemporal correlations. The frequency distributions of the original PV power plant output and the output transformed via the empirical distribution are shown in Figure 3. Figure 3 shows that the unconverted PV output exhibits pronounced non-normal and multi-modal characteristics. The data before and after transformation are presented in Table 1. By applying the empirical distribution transformation, the output data were converted into uniform variables in the range [0, 1]. This transformation effectively eliminated the skewness and multi-modality of the original PV output distribution. The parameters of the hybrid Copula model, including the weights and characteristic parameters of the four Copula functions, were estimated using the EM algorithm. ω = [0.69, 0.16, 0.10, 0.05], $\theta_C \approx 4.42$, $\rho_G \approx 0.82$, $\theta_{Gum} \approx 2.29$, $\theta_F \approx 7.43$. The log-likelihood, AIC, and BIC values of the obtained hybrid model are given in Table 2. As shown in Table 2, the hybrid Copula model achieved a log-likelihood of 9979 – an improvement of 3997, 4602.2, 5518.3, and 4815.2 over the four single Copula models, respectively. Furthermore, the AIC and BIC values of the hybrid model are significantly lower than those of all single Copula models. This indicates that the hybrid model achieves an optimal balance between goodness-of-fit and complexity, effectively capturing the joint distribution characteristics of the data.

Table 1 Transformed uniform distribution data of PV power plants

Statistic	*PV plant 1 (normalised output data)*	*PV plant 2 (normalised output data)*
count	8760	8760
mean	0.499101	0.499125
std	0.290167	0.290127
min	0.000001	0.000001
25%	0.250057	0.250057
50%	0.500000	0.500000
75%	0.749943	0.749943
max	0.999886	0.999886

Table 2 Model comparison

Model	*Log-likelihood*	*AIC*	*BIC*
Clayton	5,982.0	–11,961.9	–11,954.8
Gaussian	5,376.8	–10,751.6	–10,744.5
Gumbel	4,460.7	–8,919.4	–8,912.3
Frank	5,163.8	–10,325.0	–10,318.5
Mixed Copula	9,979.0	–19,543.0	–19,494.4

Figure 3 Frequency distribution of PV power plant output (see online version for colours)

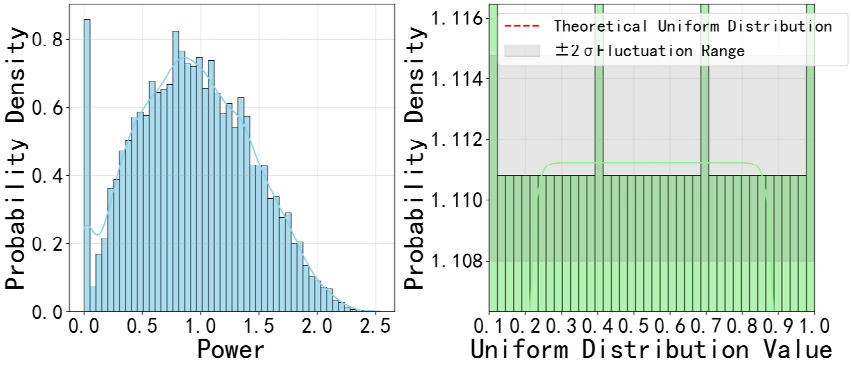

5.2 Scenario sampling and reduction

The adaptive importance sampling method was used to efficiently generate scenarios with realistic statistical characteristics from the joint distribution. By iteratively optimising the proposal distribution, the sampling efficiency for high-risk tail regions was enhanced. After systematic resampling, a total of 8,760 initial samples were obtained. Subsequently, the GMM clustering algorithm was applied for scenario reduction.

To intuitively demonstrate the efficiency gain and adaptive nature of the AIS method, we visualise its iterative optimisation process. Figure 4plots the coefficient of variation (CV) of the importance weights across AIS iterations. The CV, defined as the ratio of the standard deviation to the mean of the weights, is a key metric for sampling efficiency – a lower CV indicates a better match between the proposal and target distributions. As shown in Figure 4, the CV rapidly decreases within the first few iterations and stabilises at a low level, demonstrating that the proposal distribution is dynamically and effectively adjusted to concentrate sampling effort on high-probability regions of the target hybrid Copula distribution. This visualisation confirms that AIS significantly improves sampling efficiency over static sampling methods, particularly for capturing critical tail dependencies in PV output.

Figure 5 illustrates the variation of evaluation metrics, including the silhouette coefficient and BIC criterion, during scenario reduction. As can be seen from Figure 5, when the number of typical scenarios is 5, the BIC value is relatively low, indicating the best model fit while avoiding the risk of overfitting. A Davies-Bouldin index of 1.3 suggests good inter-cluster separation and tight intra-cluster point distribution. A

Calinski-Harabasz index of 9,000 indicates that the cluster compactness and separation still meet practical requirements. ‘Based on these metrics, the number of typical PV output scenarios was determined to be five.

Figure 4 CV of weight distribution during AIS iterative process (see online version for colours)

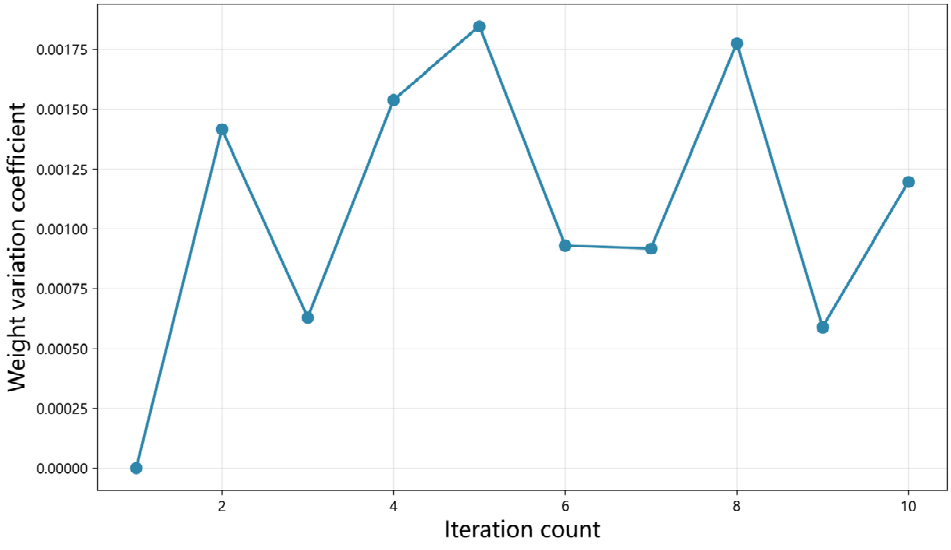

Figure 5 Clustering evaluation metrics (see online version for colours)

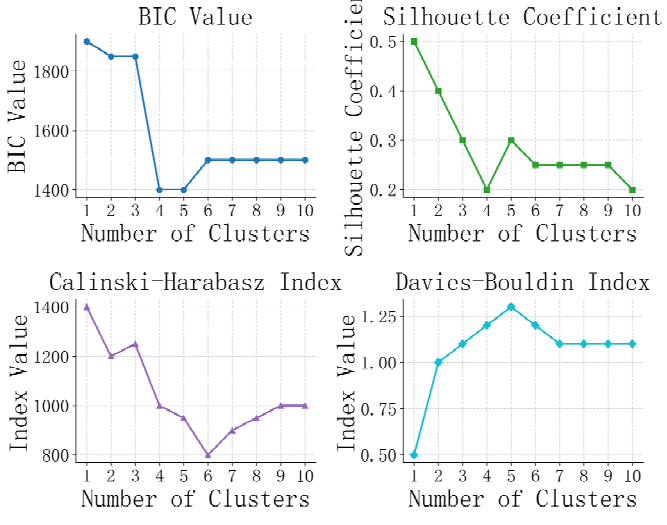

Furthermore, the occurrence probabilities of these five typical scenarios are listed in Table 3. As shown in Table 3, scenario 5 (output ≈ 0) represents extreme conditions such as nighttime or zero irradiance. Scenario 4 represents low-output conditions typical of early morning, evening, or cloudy weather. Scenario 1 corresponds to medium output, reflecting typical daily operation. Scenario 3 corresponds to high output under clear

conditions, whereas Scenario 2 represents extreme high-output cases under intense sunlight. The clustering results clearly identified multiple operational modes of PV output, whose probability distribution aligned well with historical data. This approach ensures that the set of five scenarios guarantees statistical representativeness for probabilistic power flow calculations at minimal computational cost. It also ensures that subsequent state and structural vulnerability metrics accurately reflect the system's true weaknesses across the entire spectrum of operating conditions, particularly under extreme high-risk scenarios. Consequently, this selection directly serves the ultimate goal of precise risk assessment.

Table 3 Analysis results of output correlation scenarios

Scenario	*PV1/(MW)*	*PV2/(MW)*	*Probability*
1	0.811099	1.538291	0.2330
2	1.491976	2.317817	0.2169
3	1.099047	1.844808	0.3002
4	0.413813	0.809737	0.2201
5	0	0	0.0298

5.3 Comprehensive identification of vulnerable sections in the active distribution network

5.3.1 Component state vulnerability indicators

The state vulnerability assessment indicators for each node and line are presented in Table 4. The risk value integrates both the likelihood and severity of potential violations. Analysis of Table 4 reveals that the voltage violation probabilities for nodes 10, 11, and 16 are 12.32%, 23.93%, and 97.83%, respectively. Nodes 10 and 11 share the same power supply capacity increment, highlighting the dominant role of violation probability in determining the risk. However, the risk value for node 16 (0.355) is significantly lower than that of node 11. This is because node 16 had a smaller power supply capacity increment, resulting in higher vulnerability severity. This result indicates that node 16 was operating near its limit with limited disturbance tolerance. These findings demonstrate that the proposed risk indicator effectively integrated both the likelihood and severity of potential limit violations.

The power supply capacity increment reveals the potential vulnerability of components. For instance, lines 7-8 and 8-9 have current violation probabilities of 68.12% and 53.71%, respectively, with corresponding risk values of 8.264 and 6.516. The difference in risk values arises not only from probability differences but also from the smaller power-supply capacity increment of line 7–8, indicating greater vulnerability. Notably, key feeder sections such as lines 1–2 and 2–3 showed violation probabilities of 1.0 and zero load-growth potential under all operational scenarios. These sections were identified as extremely vulnerable and require priority reinforcement.

Table 4 State vulnerability assessment indicators

Node	*Capacity increment*	*Vulnerability severity*	*Risk index*	*Node*	*Capacity increment*	*Vulnerability severity*	*Risk index*	*Line*	*Capacity increment*	*Vulnerability severity*	*Risk index*
10	4.9500	12.13132	1.49424	17	0.69575	0.10517	0.10449	1–2	0	0.1052	0.10517
								2–3			
								3–4			
								4–5			
								5–6			
11	4.9500	12.13132	2.90255	18	0.37326	0.10517	0.10472	6–7	0	0.1052	0.10225
12	3.3781	4.98384	2.35894	30	1.5844	1.44046	0.07526	7–8	4.95	12.1313	8.26414
13	1.3188	1.13695	1.04088	31	1.10625	0.92154	0.81688	8–9	4.95	12.1313	6.51612
14	0.3594	0.32272	0.30971	32	0.67188	0.54641	0.51591	9–10	4.95	12.1313	0.29027
15	0.5672	0.46755	0.45454	33	1.92031	1.88682	1.80645	23–24	4.95	0.3258	0.3258
16	0.4188	0.36257	0.35469					27–28	4.95	12.1313	12.1313

5.3.2 Component structural vulnerability indicators

The structural vulnerability assessment of components was conducted based on the improved structural vulnerability indicator system, with the evaluation results presented in Tables 5 and 6. As shown in Table 5, different indicators capture various aspects of component structure, and no single indicator fully represents their overall importance. The topological centrality and electrical centrality of nodes are not entirely consistent. Nodes 3 and 4, serving as key hubs on the network backbone, have node degree indicators of 10.828 and 5.156, and node betweenness indicators of 0.670 and 0.655, respectively, both significantly higher than the network average. However, their node injection power indicators were lower than those of the end nodes 24 and 25. This indicates that while nodes 3 and 4 are crucial in terms of topological connectivity, their transmitted power levels are relatively low under the current operating scenario. As shown in Table 6, the line supply vulnerability indicator effectively identified structural bottlenecks. The line supply vulnerability indicator for lines 16–17 is 307.47, significantly lower than that of lines 1–2. A smaller value of this indicator denotes poorer load restoration capability after a line fault and a greater impact on power supply reliability. Therefore, although lines 16–17 was not part of the traditional main feeder, its structural vulnerability suggests that reinforcement through new tie-line planning should be prioritised.

Table 5 Node structural vulnerability assessment results

Node	$D_{N,i}$	$N_{P,i}$	$B_{N,i}$	*Node*	$D_{N,i}$	$N_{P,i}$	$B_{N,i}$
1	1.54688	0.0	0.0	18	1.03125	0.21172	0.0
2	9.28125	0.25069	0.41369	19	5.15625	0.21172	0.25893
3	10.82813	0.21172	0.66964	20	4.125	0.21172	0.17857
4	5.15625	0.31003	0.65476	21	3.09375	0.21172	0.092261
5	5.15625	0.14420	0.6875	22	1.03125	0.21172	0.0
6	9.28125	0.13596	1.0	23	5.15625	0.22132	0.17857
7	5.15625	0.48068	0.6875	24	3.09375	1.0	0.09226
8	4.125	0.48068	0.65476	25	1.03125	1.0	0.0
9	4.125	0.13596	0.61607	26	5.15625	0.13973	0.52083
10	4.125	0.13596	0.57143	27	4.125	0.13973	0.46429
11	4.125	0.11626	0.52083	28	4.125	0.13596	0.40179
12	4.125	0.14932	0.46429	29	4.125	0.29864	0.33333
13	4.125	0.14932	0.40179	30	4.125	0.44886	0.25893
14	4.125	0.31003	0.33333	31	4.125	0.35583	0.17857
15	4.125	0.13076	0.25893	32	3.09375	0.5	0.09226
16	4.125	0.13596	0.17857	33	1.03125	0.15501	0.0
17	3.09375	0.13596	0.09226				

Table 6 Line structural vulnerability assessment results

Line	$D_{L,n}$	$H_{L,n}$	$B_{L,n}$	*Node*	$D_{L,n}$	$H_{L,n}$	$B_{L,n}$
1–2	0.01009	6387.278	0.04813	17–18	0.04276	710.72	0.43262
2–3	0.14274	1195.03	0.25729	18–19	0.04036	2916.23	0.10543
3–4	0.07899	1609.58	0.19102	19–20	0.24033	326.52	0.94167
4–5	0.05676	1545.79	0.19890	20–21	0.05790	1049.84	0.29287
5–6	0.19263	611.05	0.50318	21–22	0.05402	562.57	0.54655
6–7	0.11510	1022.61	0.30067	22–23	0.10509	1209.79	0.254149
7–8	0.08893	882.39	0.34845	23–24	0.11762	577.80	0.53214
8–9	0.13465	521.28	0.58984	24–25	0.05230	581.11	0.52911
9–10	0.13586	516.64	0.59514	25–26	0.04056	2901.80	0.10595
10–11	0.02198	3192.56	0.09630	26–27	0.03785	2072.94	0.14832
11–12	0.04186	1676.49	0.18340	27–28	0.14989	468.28	0.65661
12–13	0.19831	353.94	0.86871	28–29	0.11323	619.86	0.49603
13–14	0.09505	738.44	0.41638	29–30	0.06047	1160.78	0.26488
14–15	0.08399	835.62	0.36795	30–31	0.14544	482.58	0.63714
15–16	0.09811	715.41	0.42978	31–32	0.04384	1386.42	0.22177
16–17	0.19769	307.47	1.0	32–33	0.02898	1048.74	0.29318

5.3.3 Comprehensive identification of vulnerable sections in the distribution network

To validate the effectiveness of the GNN-based vulnerable section identification method proposed in this study, a comprehensive analysis was conducted from four dimensions: model convergence performance, decision-making mechanism, spatiotemporal generalisation capability, and method comparison. This constructs a complete chain of evidence, thoroughly revealing the unique advantages of the GNN model in integrating the dual ‘state-structure’ characteristics.

5.3.3.1 Model training and convergence performance analysis

Figure 6 illustrates the evolution of the model’s training performance. As shown in Figure 6, the training loss steadily decreased from an initial value of 0.5922 to a final value of 0.2237, demonstrating good convergence characteristics. The testing loss also showed a downward trend, decreasing from 0.0159 to 0.0088, indicating the model’s good generalisation capability on unseen data. When the learning rate decayed from 0.001 to 0.0005 at the 5th epoch, this adjustment effectively facilitated fine-tuning of the model, increasing the test accuracy from 80.49% to a final value of 88.00%. In terms of accuracy, the model learned rapidly in the first 5 epochs, with accuracy increasing quickly from 73.52% to 84.01%. In subsequent epochs, the model entered a stable optimisation phase, with accuracy steadily improving amidst fluctuations, eventually reaching the best performance of 88.00% at the 9th epoch. The gap between training accuracy and testing accuracy remained within a reasonable range, indicating no significant overfitting phenomenon.

Figure 6 Performance curves of the training process (see online version for colours)

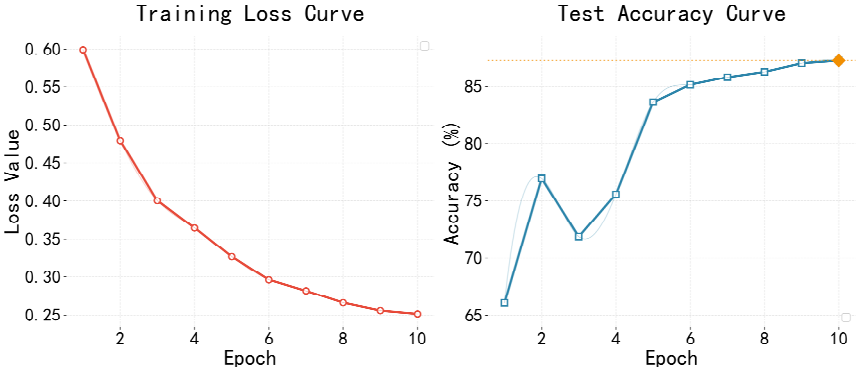

5.3.3.2 GNN decision mechanism and typical case analysis

To deeply analyse the decision-making logic of the GNN model, two types of typical nodes were selected for in-depth analysis, revealing the process by which the model integrates dual state and structural information for comprehensive judgment.

The core of our GNN's decision logic lies in its iterative message-passing mechanism, defined by equations (16)–(18). To elucidate how a node's final classification emerges, we trace the information flow for representative nodes.

For node 16 (classified as 'short-term vulnerable'): Its own state vulnerability risk (0.355) is high, while its direct topological indicators (degree: 4.125) are moderate. The key to its correct classification lies in the information aggregated from its neighbour, Line 16-17. During message passing, the feature vector of lines 16–17, which contains an extremely high structural vulnerability (supply vulnerability indicator: 307.47, the lowest in the system), is processed by the message function $\text{MLP}^{(i)}$ in equation (16). This generates a potent message signal. When aggregated to Node 16 via equation (17), this signal amplifies the node's representation in dimensions related to 'structural bottleneck risk.' After the update in equation (18), Node 16's embedding $h_{16}^{(L)}$ effectively encodes both its intrinsic state risk and the critical structural weakness of its connected line, leading the classifier to assign the 'short-term vulnerable' label. This process demonstrates that our GNN performs relational reasoning, assessing a node not in isolation but within its local network context.

For node 3 (classified as 'non-vulnerable'): Despite its high topological centrality (degree: 10.828), its state risk is low. More importantly, the messages from its strong neighbours (e.g., lines 2–3 and 3–4, which have excellent supply vulnerability indicators) provide positive information about network robustness during aggregation. The model learns that being connected to structurally resilient components mitigates risk. Thus, through multiple layers of message passing, node 3's representation incorporates this stabilising neighbourhood information, correctly overriding a potential overestimation of vulnerability based on topology alone.

This text-based mechanistic explanation shows that our GNN's decisions are not opaque but are grounded in a understandable, step-wise fusion of multi-hop neighbourhood information, directly mirroring the physical propagation of disturbances in a power network.

5.3.3.3 *Feature importance analysis and spatiotemporal generalisation capability*

To further elucidate the GNN model's decision mechanism, a gradient-based feature importance analysis method was employed. Table 7 presents the quantified contribution of each feature to vulnerable section identification. As shown in Table 7, among node features, the state vulnerability risk indicator and the node degree indicator contributed the most (28.3% and 22.1% respectively), indicating the significant impact of fusing state and structural features for assessing node vulnerability. For line features, the line current violation risk and the line supply vulnerability indicator dominated the contributions (32.8% and 27.4% respectively), highlighting that electrical safety constraints and topological criticality are core factors for judging line vulnerability. Furthermore, the GNN automatically learns distribution network topology information through message passing and neighbourhood aggregation, acquiring implicit topological features that effectively enhance the identification capability for vulnerable nodes. This also exemplifies the unique advantage of GNNs in capturing complex network effects.

The gradient-based method, which computes the sensitivity of the model's output prediction with respect to input features, provides a computationally efficient means of feature attribution. However, its application to GNNs warrants careful consideration of potential limitations. In deep GNNs with multiple nonlinear layers, the gradients can saturate (e.g., vanish or explode) during backpropagation, especially when using activation functions like ReLU, which may lead to underestimation of the importance of certain features. Furthermore, the composite nature of the GNN's message-passing mechanism means that gradients attributed to a node's features also inherently encode indirect influences from its multi-hop neighbours, potentially introducing attribution bias when disentangling purely local effects.

Table 7 Feature Importance analysis results

Feature type	*Feature name*	*Importance (%)*
Node features	Voltage violation risk	28.3
	Node degree indicator	22.1
	Node injection power indicator	18.7
	Node betweenness indicator	16.5
	Voltage magnitude	9.2
	Voltage phase angle	5.2
Edge features	Current violation risk	32.8
	Line supply vulnerability indicator	27.4
	Line degree indicator	21.5
	Line betweenness indicator	18.3

In the context of this study, several factors mitigate these concerns and support the use of gradient-based analysis as a meaningful explanatory tool. First, our hybrid temporal-GNN architecture (a two-layer bidirectional LSTM followed by three GCN layers) uses ReLU activation in the graph convolutional layers, which, despite its potential for zero gradients, is paired with a moderate-depth architecture (total of 5 trainable layers) that does not severely hinder gradient flow. Second, the bidirectional LSTM captures temporal dependencies before graph convolutions, which helps stabilise

the gradients by providing richer initial node representations. Third, the primary purpose of this analysis is not to obtain perfectly disentangled feature attributions, but to identify which high-level feature categories (e.g., state risk vs. structural centrality) play dominant roles in the model's decision-making—a task for which gradient-based saliency has been shown to be reliable in practice, especially when the model architecture is not excessively deep.

We acknowledge that gradient-based methods are one of several possible approaches to explainability, and that techniques such as SHapley Additive exPlanations (SHAP) or GNN-specific explainers (e.g., GNNExplainer) could provide complementary perspectives. However, given the scope of this paper and the corroboration of our gradient-based findings with engineering intuition (e.g., the prominence of voltage violation risk in node classification), we believe the presented analysis offers a valid and insightful characterisation of the GNN's decision logic. Future work could systematically compare multiple explanation methods for GNNs in power system applications.

Table 8 presents the model's identification performance differences across various time periods and network areas, further revealing its generalisation capability. As shown in Table 9, the model achieved its highest accuracy of 90.5% during PV peak hours, primarily because the operational state variations caused by PV output fluctuations during this period provided richer discriminatory information. Spatially, the PV integration area posed the greatest identification challenge, with an accuracy of 85.3%, reflecting the complex impact of distributed PV integration on traditional distribution network operation characteristics. The above analysis further demonstrates the GNN model's capability in spatiotemporal pattern recognition when processing time-series graph data.

Table 8 Spatiotemporal performance analysis

Temporal characteristics				
Metric	*Daytime (6:00~18:00)*	*Nighttime (18:00~6:00)*	*PV peak period*	*Load peak period*
Accuracy (%)	89.2	86.3	90.5	87.8
Sample size	144,182	144,139	72,105	71,980
Proportion of vulnerable nodes (%)	34.1	29.8	38.2	33.5
Spatial regions				
Metric	*PV integration area*	*Network periphery area*	*Main feeder area*	
Accuracy (%)	85.3	91.2	88.7	
Number of vulnerable nodes	12,450	8,732	13,115	
Identification difficulty	High	Medium	Medium	

5.3.3.4 Comparative experiment and comprehensive advantage demonstration

To comprehensively evaluate the model's capability in identifying vulnerable nodes, this paper compares the GNN method with an improved least squares support vector machine (LSSVM) method. LSSVM is chosen as it is a well-established, kernel-based method effective for small-to-medium-sized, high-dimensional classification problems common

in power systems, and it serves as a strong representative of non-graph-based approaches. The performance comparison of the two methods, based on evaluation results from 288,321 test samples, is shown in Table 9. As seen in Table 9, the GNN method achieved an accuracy of 88.00%, which is an increase of 19.62 percentage points (or 28.7%) compared to the LSSVM's 68.38%. In terms of precision, GNN reached 88.15%, while LSSVM was only 46.76%, indicating a significant advantage for GNN in reducing false positives. The recall metric shows that GNN could more comprehensively identify actual vulnerable sections, and the F1-score of 0.8806 further confirms a good balance between precision and recall for GNN. Regarding efficiency, the average inference time for GNN was 0.8598 ms/sample, significantly lower than LSSVM's 10.7226 ms/sample, representing an efficiency improvement of approximately 12.5 times. This indicates that GNN is not only superior in accuracy but also more practical in application scenarios requiring high real-time performance.

Table 9 Comparison of identification performance metrics

Method	*Accuracy (%)*	*Precision (%)*	*Recall (%)*	*F1-score*
LSSVM	68.38	46.76	68.38	0.5554
GNN	88	88.15	88	0.8806

The aforementioned comparative results demonstrate that the GNN-based vulnerable section identification method proposed in this paper significantly outperforms the traditional LSSVM method across multiple dimensions. This performance advantage primarily stems from the following two aspects: First, the GNN method can effectively integrate the dual information of the distribution network's topological structure and operational state. Through the message-passing mechanism, the model can capture the electrical coupling relationships between nodes, thereby more accurately identifying vulnerable sections affected by PV output fluctuations. In contrast, the LSSVM method can only process isolated feature vectors and cannot fully utilise network topology information, limiting its identification accuracy. Second, the comprehensive evaluation indicator system constructed in this paper provides rich discriminatory features for the GNN model. The state vulnerability indicators quantify the real-time operational risk of components, while the structural vulnerability indicators reveal the inherent vulnerability attributes of the network. The effective combination of these two provides multi-dimensional, complementary bases for the model's discrimination. The feature importance analysis results (Table 7) further validate the effectiveness of this dual-feature fusion. Furthermore, the significant advantage of the GNN method in inference efficiency indicates its potential for engineering applications, capable of meeting the requirements for real-time security assessment in active distribution networks. In summary, the proposed method not only achieves high identification accuracy but also possesses good practicality and scalability.

6 Conclusions

This study addresses the challenge of identifying vulnerable sections in distribution networks with high-penetration DPVs by proposing a comprehensive assessment method that integrates hybrid Copula theory and GNNs. The main conclusions and contributions are as follows:

1 A typical scenario generation framework for PV output based on a hybrid Copula model and adaptive importance sampling was developed. The framework accurately characterised the nonlinear and asymmetric tail dependencies between PV outputs. Compared with single Copula models, the log-likelihood value increased by 60.1%, providing a reliable scenario basis for accurate system risk assessment.

2 A comprehensive vulnerability evaluation system integrating both state and structural features was constructed. At the state level, utility theory was introduced into power supply capability assessment, leading to a risk quantification method based on improved repetitive power flow. At the structural level, traditional complex network indicators were refined by incorporating the characteristics of radial distribution networks. A line supply vulnerability indicator with clear physical significance was proposed, enabling a multi-dimensional assessment of operational risk and topological criticality.

3 An end-to-end intelligent identification model for vulnerable sections based on GNNs was designed, fully leveraging the inherent graph structure of distribution networks. The message-passing mechanism effectively integrated topological connectivity with multivariate operational features, overcoming the limitations of traditional machine learning methods in processing structural information.

This research provides a complete solution – from fine-grained modelling to intelligent identification – for security assessment of distribution networks with high-penetration distributed PV, offering both theoretical value and practical engineering applicability. Future work will explore dynamic GNN architectures and extend the method to multi-energy coupled scenarios, aiming to further enhance the real-time performance and adaptability of vulnerable section identification.

Funding

The work was funded by the Science and Technology Project of State Grid Fujian Electric Power Co. Ltd. (Grand No. 52132025000B).

Declarations

All authors declare that they have no conflicts of interest.

References

Bao, D., Gao, F., Wang, P. et al. (2023) ‘Research and predictive analysis of blade load correlation based on copula function’, *Acta Energiae Solaris Sinica*, Vol. 44, No. 12, pp.323–329.

Chen, C., Zhou, Y., Chi, M. et al. (2022a) ‘A review of vulnerability research for large-scale power grids based on complex network theory’, *Control and Decision*, Vol. 37, No. 4, pp.782–798.

Chen, L., Liu, L., Zhou, C. et al. (2022b) ‘Weak link identification of integrated energy systems considering operational risk and resilience’, *Automation of Electric Power Systems*, Vol. 46, No. 6, pp.48–57.

Dong, X., Hua, Z., Shang, L. et al. (2021) 'Morphological characteristics and technical prospects of new distribution systems', *High Voltage Engineering*, Vol. 47, No. 9, pp.3021–3035.

Duan, S.M., Miao, S.H., Huo, X.S. et al. (2019) 'Modeling and dynamic correlation analysis of combined wind and solar power output based on dynamic copula', *Power System Protection and Control*, Vol. 47, No. 5, pp.35–42.

Hu, B., Xie, K., Shao, C. et al. (2023) 'Review on risks of new power systems under dual-carbon goals: characteristics, indicators, and assessment methods', *Automation of Electric Power Systems*, Vol. 47, No. 5, pp.1–15.

Liu, R. (2012) *Research on Some Fundamental Theories and Algorithms for Power System Operation Security*, PhD dissertation, North China Electric Power University.

Sun, Y., Cheng, K., Xu, Q. et al. (2022) Identification of weak links in active distribution networks considering correlation of photovoltaic output', *Automation of Electric Power Systems*, Vol. 46, No. 15, pp.96–103.

Tao, C. (2024) 'Identification of weak links in integrated electricity-gas energy systems based on time petri nets', *Electrical Measurement & Instrumentation*, Vol. 61, No. 5, pp.1–8.

Wang, B., Wang, H., Zhu, D. et al. (2022) 'A weak point identification method for integrated energy systems based on unified power flow big data', *Automation of Electric Power Systems*, Vol. 46, No. 7, pp.85–93.

Wang, C., Wang, X., Cao, Y. et al. (2024) 'Identification of key vulnerable links in power systems based on improved graph attention network', *Power System Protection and Control*, Vol. 52, No. 15, pp.36–45.

Wang, Z., Miao, S., Guo, S. et al. (2021) 'Node vulnerability assessment of distribution network considering stochastic characteristics of distributed generation output', *Electric Power Automation Equipment*, Vol. 41, No. 8, pp.33–40.

Xu, Y., Dong, S., Mao, H. et al. (2020) 'Probabilistic analysis and application of voltage stability index for distribution network based on unscented transformation method', *Proceedings of the CSEE*, Vol. 40, No. S1, pp.47–55.

Yan, G. and Li, Z. (2024) 'Construction of an outlier-immune data-driven power flow model for model-absent distribution systems', *IEEE Transactions on Power Systems*, Vol. 39, No. 6, pp.7449–7452.

Yan, M., Yu, M., Wan, K. et al. (2024) 'Vulnerability assessment of cyber-physical systems for microgrids with wind power integration against cyber attacks', *Automation of Electric Power Systems*, Vol. 48, No. 24, pp.88–100.

Yan, Z. and Xu, Y. (2024) 'A hybrid data-driven method for fast solution of security-constrained optimal power flow', *2024 IEEE Power & Energy Society General Meeting (PESGM)*, Seattle, WA, USA, pp.1–11.

Yang, J., Shang, L., Ye, X. et al. (2025a) 'Voltage weak node identification method considering distribution network fault reconfiguration', *Electric Power Engineering Technology*, Vol. 44, No. 1, pp.39–49.

Yang, M., Hu, Y., Qian, H. et al. (2025b) 'Distributionally robust optimization of integrated energy distribution network considering wind power, photovoltaics, demand response, and vine copula uncertainty', *Electrical Measurement & Instrumentation*, Vol. 62, No. 10, pp.147–155.

Yang, L., Ren, X., Cai, Z. et al. (2024) 'A review of voltage control strategies for distribution networks with high photovoltaic penetration', *Power System Technology*, Vol. 48, No. 12, pp.5056–5070.

Yu, Y., Wang, C., Li, Y. et al. (2024) 'Multi-level reverse overload risk assessment of distribution network with high penetration of PV', *High Voltage Engineering*, Vol. 50, No. 10, pp.4540–4549.

Zeng, L., Yao, W., Ai, X. et al. (2020) 'Identification of weak lines in power grid considering transient stability constraints based on double Q-learning', *Proceedings of the CSEE*, Vol. 40, No. 8, pp.2429–2441.

Zhang, M., Mou, L. and Liu, H. (2023) 'Voltage stability analysis of DC regional distribution network', *Proceedings of the CSU-EPSA*, Vol. 35, No. 7, pp.1–9+35.

Zhang, W., Sheng, W., Liu, K. et al. (2021) 'Operational risk assessment of distribution network with high-penetration distributed generation integrated based on node criticality', *High Voltage Engineering*, Vol. 47, No. 3, pp.937–947.

Zhu, X., Jin, H. and Wang, Y. (2019) 'Modeling of power dependence structure for photovoltaic power stations based on Gaussian mixture model and copula function', *Acta Energiae Solaris Sinica*, Vol. 40, No. 7, pp.1912–1919.